Video-rate three-dimensional optical coherence tomography

Markus Laubscher, Mathieu Ducros*, Boris Karamata, Theo Lasser and René Salathé
Institute of Applied Optics, Swiss Federal Institute of Technology, CH-1015 Lausanne, Switzerland
Markus.Laubscher@epfl.ch
** now with the Ophthalmology Department, The University of British Columbia, Vancouver British Columbia, Canada, V5Z 3N9*

Abstract: Most current optical coherence tomography systems provide two-dimensional cross-sectional or *en face* images. Successive adjacent images have to be acquired to reconstruct three-dimensional objects, which can be time consuming. Here we demonstrate three-dimensional optical coherence tomography (3D OCT) at video rate. A 58 by 58 smart-pixel detector array was employed. A sample volume of 210x210x80 μm^3 (corresponding to 58x58x58 voxels) was imaged at 25 Hz. The longitudinal and transverse resolutions are 3 µm and 9 µm respectively. The sensitivity of the system was 76 dB. Video rate 3D OCT is illustrated by movies of a strand of hair undergoing fast thermal damage.

OCIS codes: (170.4500) Optical coherence tomography; (170.3880) Medical and biological imaging; (120.3890) Medical optics instrumentation; (170.6900) Three-dimensional microscopy; (110.6880) Three-dimensional image acquisition

References and Links

1. M. E. Brezinski and J. G. Fujimoto, "Optical coherence tomography: high-resolution imaging in nontransparent tissue," IEEE J. Selec. Top. Quant. Electron. **5**, 1185-1192 (1999)
2. A. F. Fercher, "Optical Coherence Tomography," J. Biomed. Opt. **1**, 157-173 (1996)
3. J. M. Schmitt, "Optical Coherence Tomography (OCT): A Review," IEEE J. Selec. Top. Quant. Electron. **5**, 1205-1215 (1999)
4. W. Drexler, U. Morgner, F. X. Kartner, C. Pitris, S. A. Boppart, X. D. Li, E. P. Ippen, and J. G. Fujimoto, "In vivo ultrahigh-resolution optical coherence tomography," Opt. Lett. **24**, 1221-1223 (1999)
5. A. M. Rollins, M. D. Kulkarni, S. Yazdanfar, R. Ung-arunyawee, and J. A. Izatt, "In vivo video rate optical coherence tomography," Opt. Express **3**, 219-229 (1998), http://www.opticsexpress.org/abstract.cfm?URI=OPEX-3-6-219
6. J. Szydlo, N. Delachenal, R. Giannotti, R. Walti, H. Bleuler, and R. P. Salathe, "Air-turbine driven optical low-coherence reflectometry at 28.6- kHz scan repetition rate," Opt. Commun. **154**, 1-4 (1998)
7. M. J. Everett, K. Schoenenberger, B. W. Colston, and L. B. Da Silva, "Birefringence characterization of biological tissue by use of optical coherence tomography," Opt. Lett. **23**, 228-230 (1998)
8. J. F. deBoer, T. E. Milner, M. J. C. vanGemert, and J. S. Nelson, "Two-dimensional birefringence imaging in biological tissue by polarization-sensitive optical coherence tomography," Opt. Lett. **22**, 934-936 (1997)
9. X. J. Wang, T. E. Milner, and J. S. Nelson, "Characterization of Fluid-Flow Velocity by Optical Doppler Tomography," Opt. Lett. **20**, 1337-1339 (1995)
10. J. K. Barton, J. A. Izatt, M. D. Kulkarni, S. Yazdanfar, and A. J. Welch, "Three-dimensional reconstruction of blood vessels from in vivo color Doppler optical coherence tomography images," Dermatology **198**, 355-361 (1999)
11. Y. Pan and D. Farkas, "Non-invasive Imaging of Living Human Skin with Dual-wavelength Optical Coherence Tomography in Two and Three Dimensions," J. Biomed. Opt. **3**, 446-455 (1998)
12. J. M. Herrmann, M. E. Brezinski, B. E. Bouma, S. A. Boppart, C. Pitris, J. F. Southern, and J. G. Fujimoto, "Two- and three-dimensional high-resolution imaging of the human oviduct with optical coherence tomography," Fertil. Steril. **70**, 155-158 (1998)
13. A. G. Podoleanu, J. A. Rogers, and D. A. Jackson, "Three dimensional OCT images from retina and skin," Opt. Express **7**, 292-298 (2000), http://www.opticsexpress.org/abstract.cfm?URI=OPEX-7-9-292
14. B. M. Hoeling, A. D. Fernandez, R. C. Haskell, E. Huang, W. R. Myers, D. C. Petersen, S. E. Ungersma, R. Y. Wang, M. E. Williams, and S. E. Fraser, "An optical coherence microscope for 3-dimensional imaging in developmental biology," Opt. Express **6**, 136-146 (2000), http://www.opticsexpress.org/abstract.cfm?URI=OPEX-6-7-136

#970 - $15.00 US Received March 05, 2002; Revised May 03, 2002

15. E. Beaurepaire, A. C. Boccara, M. Lebec, L. Blanchot, and H. Saint-Jalmes, "Full-field optical coherence microscopy," Opt. Lett. **23**, 244-246 (1998)
16. A. Knüttel, J. M. Schmitt, and J. R. Knutson, "Low-coherence reflectometry for stationary lateral and depth profiling with acousto-optic deflectors and a CCD camera," Opt. Lett. **19**, 302-304 (1994)
17. S. Bourquin, P. Seitz, and R. P. Salathé, "Optical coherence topography based on a two-dimensional smart detector array," Opt. Lett. **26**, 512-514 (2001)
18. S. Bourquin, V. Monterosso, P. Seitz, and R. P. Salathé, "Video rate optical low-coherence reflectometry based on a linear smart detector array," Opt. Lett. **25**, 102-104 (2000)
19. M. Ducros, M. Laubscher, B. Karamata, S. Bourquin, T. Lasser, and R. P. Salathe, "Parallel optical coherence tomography in scattering samples using a two-dimensional smart-pixel detector array," Opt. Commun. **202**, 29-35 (2002)
20. J. A. Izatt, M. R. Hee, G. M. Owen, E. A. Swanson, and J. G. Fujimoto, "Optical coherence microscopy in scattering media," Opt. Lett. **19**, 590-2 (1994)
21. E. A. Swanson, D. Huang, M. R. Hee, J. G. Fujimoto, C. P. Lin, and C. A. Puliafito, "High-speed optical coherence domain reflectometry," Opt. Lett. **17**, 151-3 (1992)
22. P. Thevenaz and M. Unser, "High-Quality Isosurface Rendering with Exact Gradient," in *Proceedings of The 2001 IEEE International Conference on Image Processing (ICIP'01)*, **1**, 854-857 (2001).

1. Introduction

Over the past 15 years the biomedical imaging technique called optical coherence tomography (OCT) has experienced many technological improvements and found a host of useful applicationss [1-3]. The main aspects of development have been spatial resolution [4], sensitivity and acquisition speed [5,6]. In addition, new implementations of OCT have been developed that provide additional information about the sample under study. For example, polarization-sensitive OCT allows the measurement of depth-resolved sample birefringence [7,8] and Doppler OCT permits the assessment of flow velocity in biological samples [9]. However, acquiring two-dimensional OCT images is not sufficient to fully describe the three-dimensional morphology of biological samples under study. For example, three-dimensional OCT images would be required to measure the depth and lateral extent of epithelial tumors in the skin, cervix or oral mucosa. A few research groups reported the reconstruction of three-dimensional maps of reflectivity obtained by acquiring two-dimensional arrays of adjacent OCT A-scans, but such a procedure can be time consuming[10-12].

Besides the “classic” longitudinal OCT imaging technique based on A-scans, two classes of *en face* (transversal) OCT imaging techniques have been proposed: the “flying spot” and the “parallel OCT” techniques. Both can be used to acquire three-dimensional reflectivity maps. In the “flying spot” technique the probing light beam is scanned transversally in raster scans to acquire *en face* images at different depths [13,14] whereas in the “parallel OCT” technique wide-field illumination and acquisition is used [15-17]. The detectors employed in the latter technique are photodetector arrays in contrast to all other OCT techniques which rely on single-unit detectors. The need for lateral scanning is in this case eliminated, to the advantage of higher acquisition rates.

Charge coupled device (CCD) cameras are the most commonly used imaging devices for parallel imaging schemes. However, CCD cameras suffer from two drawbacks when used in parallel OCT systems: (1) the high optical DC intensity reflected by the reference mirror reduces the dynamic range available for AC interferometric signal detection, (2) the CCD frame rate (typically ~100 Hz for 512x512 pixels) is much lower than the interferometric signal frequency (typically greater than 1 kHz). In this case a lock-in detection or synchronous illumination scheme has to be employed [15], which limits the image acquisition speed. A different photodetector array based on CMOS technology was specifically developed for parallel OCT [17,18]. Besides transducing light signals into electrical signals, CMOS detectors offer the additional functionality of customized, integrated signal processing for each pixel. Optical coherence tomography with a parallel detection scheme using such one- and two-dimensional smart pixel detector arrays (SPDA) was previously demonstrated on reflective surfaces [17]. Recently, we have shown the feasibility of using a SPDA in scattering

#970 - $15.00 US Received March 05, 2002; Revised May 03, 2002

samples as well [19]. In the present work we use a SPDA to demonstrate for the first time to our knowledge 3D OCT imaging at video-rate.

2. Method

2.1 Optical set-up

The optical set-up is illustrated in Figure 1. The light source employed is a compact femtosecond mode-locked Ti:Sapphire laser (MLTS) (FemtoLasers Inc., Vienna, Austria) with a nearly Gaussian spectrum centered at 800 nm and a full-width-at-half-maximum (FWHM) spectral bandwidth of 100 nm. Lenses L1 and L2 form a telescope to increase the beam diameter before it enters a free space Michelson interferometer. An average power of 430 mW is available at the interferometer input. A beamsplitter cube (BS) separates the light into the interferometer reference and sample arms. A variable neutral density filter wheel (F) is placed into the reference arm and a compensation glass plate (C) of equal thickness into the reference arm. Two identical microscope objectives (L4 and L5, 20x) are used to illuminate and collect reflected light from the sample (S) and reference mirror (RM). The incident average power on the sample is 120 mW. The illumination profile on the sample is approximately gaussian and covers the square field of view of the detector of 210x210μm^2. Light reflected from S and RM interferes only if the optical path lengths match to within the source coherence length. RM is translated longitudinally using a voice-coil scanning stage (Physik Instrumente (PI) GmbH & Co) that is driven by a triangular input function at a frequency of 12.5 Hz. The scan amplitude is 80μm, as measured by the voice coil stage encoder. Acquisition is performed both during the forward and backward half-period of the triangular scan, i.e. at 25 Hz. The sample is imaged by lens L6 onto a SPDA with 58x58 pixels. Each pixel consists of a silicon photodiode coupled to a CMOS electronic circuit that amplifies and demodulates AC signals [17]. Each pixel output provides an analog voltage proportional to the envelope of the optical interference signal. The analog signals corresponding to each pixel are read out sequentially at a rate of 5 MHz, digitized by a 12-bit A/D card and displayed on a computer screen. Volumetric datasets with 58x58x58 pixels, corresponding to 210x210x80 μm^3 are thus acquired at a rate of 25 Hz.

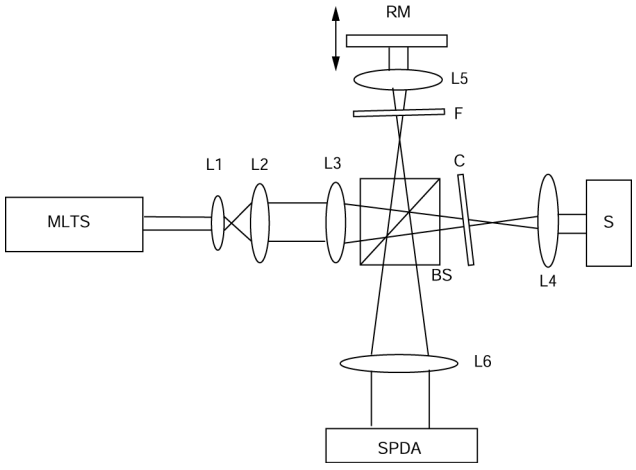

Fig. 1. Parallel OCT optical setup schematic. The different elements are: mode-locked Ti:Sapphire femtosecond laser (MLTS); achromatic lenses (L1, L2, L3, and L6); non-polarizing achromatic beamsplitter cube (BS); identical achromatic microscope objectives 20X, 0.45 NA (L4 and L5); reference mirror (RM); variable neutral density filter wheel (F); compensation glass plate (C); 58 by 58 smart pixel detector array (SPDA) and sample (S).

#970 - $15.00 US Received March 05, 2002; Revised May 03, 2002

2.2. Sample

The sample was a strand of dark human hair on a microscope glass slide positioned at the focal plane of the microscope objective L4. The average irradiance incident on the sample is approximately 173 W/cm^2. Because of the high melanin concentration in the hair strand the illuminating laser beam is strongly absorbed. As the hair is only in contact with a glass plate and with the air the heat transfer to the surrounding media is rather low and the accumulated thermal energy causes the hair to swell and to burn. Only because of the high absorption coefficient of the imaged sample do we observe an interaction between the probing laser beam and the sample. Indeed, we have observed light-colored hair and onions under identical conditions and no damage to the sample was observed. Even though the total power used for sample illumination is high (120 mW) the irradiance remains relatively low. Indeed, the employed average irradiance is inferior to irradiance reported in literature in point by point scanning OCT systems using femtosecond lasers[4]. Nevertheless, thermal effects, depending on irradiance, pulse length, exposition duration, tissue absorption coefficient and thermal properties, should be investigated for each specific sample.

3. Results

3.1. System performance

We measured the system longitudinal response on a mirror in air to be 3 μm (FWHM), which is in good agreement with the theoretically expected value for a Gaussian spectrum of 100 nm bandwidth at a central wavelength of 800 nm. Transverse resolution in air was determined using a USAF resolution target at the focal plane of L4. Using the 20x objectives we could resolve reflective bars with a maximum spatial frequency of 114 mm^{-1}, corresponding to a transverse resolution of 8.8 μm. The transverse resolution is limited by the NA of the microscope objectives (0.45) and the fill factor of the detector array (10%).

To measure the system sensitivity we imaged an air-water interface (2% power reflection) and varied the attenuation of the reference arm intensity by rotating the neutral density filter wheel F until the detector signal was maximized to a value that we call $V_{2\%\ max}$. The sensitivity S in decibel of the system is then given by

$$S = 20\log\frac{V_{2\%\max}}{\sigma} + 10\log\frac{1}{0.02} \qquad (1)$$

where σ is the electronic signal noise that is experimentally taken to be the standard deviation of all voxels values when no sample was present. The sensitivity was measured to be 76 dB. During all experiments on biological samples, such as the hair strand, the neutral density filter wheel stayed at the same position.

The advantages of using the method described above to measure the system sensitivity are threefold: (1) The sample (water) mimics typical biological samples reflectivities; (2) The electronic AC gain of the SPDA detector depends on the level of optical DC illumination. The lower the DC illumination the higher the AC gain. Therefore, by decreasing the reference arm intensity the AC gain is increased more than the optical AC signal is attenuated and thus a higher electric output signal can be obtained; (3) By decreasing the optical DC illumination the noise decreases and approaches the shot noise limit.

The maximum SNR of an OCT system is reached when (1) the detection is shot noise limited and (2) the detection bandwidth matches the interferometric signal bandwidth [20,21]. In the present experimental conditions we calculated the optimum SNR to be 92 dB. However, the current implementation of the electronic filter integrated in each pixel (110x110 μm^2) of the SPDA does not allow a very fine filtering of the signal. We estimated the filtering bandwidth to about 40 kHz. The shot noise limited SNR of our setup is then 77.6 dB which is close to the measured SNR.

#970 - $15.00 US Received March 05, 2002; Revised May 03, 2002

3.2. Sample images

In the following we reproduce image data that has been acquired during a 1600 ms time interval at a rate of 25 volumes per second, i.e. a time sequence of 40 volumetric data sets with dimensions of 58x58x58 voxels each. The raw data is in the form of a one-dimensional array of 58x58x58x40 16-bit integers from which we have reconstructed the following two- and three-dimensional images and movies.

Figure 2 shows a schematic of the imaged volume in relation to the sample and three tomographic images along the sample symmetry axes at the beginning of the time sequence. The image size format has been adjusted to represent the true geometric dimensions of 210x210 μm^2 and 210x80 μm^2, respectively. All images are shown in inverted grayscale reflectivity coding. The *en face* image (center) shows the shadow caused by the hair at the height of the supporting glass plate. On the longitudinal cut (right top), taken parallel to and at the center of the hair strand, one distinguishes its upper and lower surfaces. The cross-sectional cut (right bottom) exhibits the profile of the hair on the glass plate.

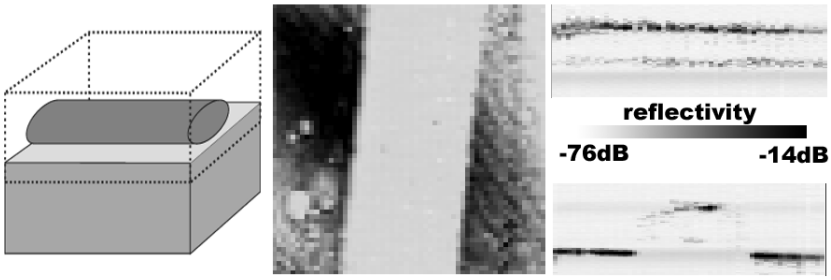

Fig. 2. (left) Schematic of the imaged volume (dashed parallelepiped) in relation to the sample (hair strand on glass slide). (center) *En face* image (210x210 μm^2) at the height of the contact between hair and glass. (right top) Longitudinal cut (210x80 μm^2) parallel to and at the center of the hair. (right bottom) Cross-sectional cut (210x80 μm^2) perpendicular to the axis of the hair strand.

The reflectivity scale bar of Figure 2 also applies to all following tomographic images which we represent for simplicity in a square 58x58 pixel image format. Figure 3 is a movie that shows the temporal evolution of the sample in the three tomographic planes previously discussed. During the first 960 ms (24 time frames) no modification of the hair is visible. The incident laser radiation is highly absorbed and locally heats up the hair strand. At frame 25 (1000 ms after the beginning of irradiation) first modifications become noticeable in the longitudinal and cross-sectional cuts. We see locally some higher reflectivity signals from inside the hair volume, to the detriment of the signal corresponding to the lower side of the hair that starts to be shadowed by these new backscattering sites. On the *en face* image these changes are not yet visible, because the interaction between the laser and the hair has up to this moment not progressed far enough in depth to modify the hair's shadow on the glass plate. On the next frame (40 ms later) a burn crater in the center of the hair can clearly be distinguished on the longitudinal and cross-sectional cuts. Its depth can be estimated to approximately 45% of the hair's thickness. The formerly smooth surface of the hair becomes very fragmented and scattering in the area of the burn crater and the signals from the lower hair surface disappear because of shadowing. Reflectivity signals from above the former position of the hair appear and might be identified as debris. The localization of the laser-hair interaction to the center of the optical field is due to the Gaussian like spatial intensity profile of the probing laser beam. Note that the SPDA cannot compensate for non-uniform illumination since settings are common to all pixels. The area of interaction can be measured to be of a diameter of about 120-130 μm. On the next frame (40 ms later) the hair's modifications become finally visible on the *en face* image. The hair starts to swell laterally into a bulb and continues doing so for the next 520 ms until the end of the acquisition. This bulb attains approximately 150% of the hair's original width. The swelling can of course be

#970 - $15.00 US Received March 05, 2002; Revised May 03, 2002

observed on the cross-sectional images as well. However, other than the lateral swelling no other major modifications are visible in this final phase of the interaction.

Fig. 3. (149 kB) Tomographic images acquired during a 1600ms time interval at a rate of 25 volumes per second (40 time frames). (left) *En face* image (210x210 μm^2) at the height of the contact between hair and glass. (center) Cross-sectional cut (210x80 μm^2). (right) Longitudinal cut (210x80 μm^2) parallel to and at the center of the hair. Reflectivity grayscale as in Figure 2.

Because of an experimental problem of synchronization images of even and odd volumes are slightly shifted in relation to each other, which causes the image jumps on this movie. This imperfection can easily be corrected for and this has been done in Figure 4. Furthermore, the last column of photodetectors (rightmost column of pixels on an *en face* image) exhibits a markedly different response than the others, which causes image artifacts. This is due to a different electronic pixel layout that has been realized on the last column for experimental purposes. The distortions visible on adjacent columns in the beginning of the time sequence (clearly visible as trailing signals of the glass plate on the cross-sectional cuts) might be related.

Figure 3 illustrates three tomographic views that permit to visualize relatively well the dynamic phenomenon observed. However, much more data has been acquired with this 3D OCT method and any chosen view could be visualized. In order to allow an inspection of the entire volume at one glance we use the whole data set to generate a three-dimensionally rendered representation based on isosurfaces. Each of the 40 time frames has been rendered as described in [22] and combined into the movie shown in Figure 4. This representation goes far beyond tomographic images and is very useful for localizing regions of particular interest.

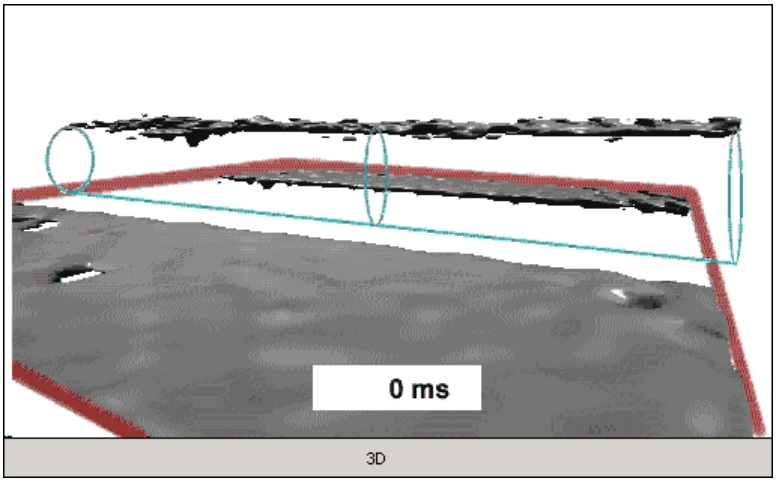

Fig.4. (740 kB) Movie of a 3D rendering of the sample based on isosurfaces. To facilitate the comprehension of this particular perspective we indicate the situation of the hair and the glass slide by the colored lines in the first frame.

#970 - $15.00 US
Received March 05, 2002; Revised May 03, 2002

4. Conclusion

In conclusion, we have implemented a parallel OCT system capable of 3D data acquisition at video-rate. The key element of the system is a smart pixel detector array, conceived and developed specifically for *en face* OCT imaging. Combined with a femtosecond light source and a microscopic imaging scheme this system allows for both high longitudinal and transverse resolutions when limited to a small sample volume. We have illustrated its performance by imaging the time-resolved thermal damage of a strand of dark human hair under the influence of the probing laser beam. Besides tomographic images we have also shown a three-dimensionally rendered movie.

Acknowledgments

We would like to thank P. Thevenaz for his help in the 3D rendering of our data and S. Bourquin for valuable discussions.

#970 - $15.00 US Received March 05, 2002; Revised May 03, 2002